ADVANCED FUNCTIONAL MATERIALS
www.afm-journal.de

Self-Driven Metal–Semiconductor–Metal WSe_2 Photodetector with Asymmetric Contact Geometries

Changjian Zhou, Salahuddin Raju, Bin Li, Mansun Chan, Yang Chai, and Cary Y. Yang*

Self-driven photodetectors have wide applications in wireless sensor networks and wearable physiological monitoring systems. While 2D materials have different bandgaps for potential novel application fields, the self-driven photodetectors are mainly built on PN junctions or heterostructures, whose fabrication involves doping or reliable multiple transfer steps. In this study, a novel metal–semiconductor–metal (MSM) WSe_2 photodetector with asymmetric contact geometries is proposed. A high responsivity of 2.31 A W^{-1} is obtained under zero bias, and a large open-circuit voltage of 0.42 V is achieved for an MSM photodetector with a large contact length difference. The MSM photodetector can overcome the disadvantage of high dark current in traditional MSM photodetectors. A small dark current of ≈1 fA along with a high detectivity of 9.16×10^{11} Jones is achieved. The working principles and finite element analysis are presented to explain the origin of the self-driven property and its dependence on the degree of asymmetry.

1. Introduction

Photodetectors are widely used in optical-fiber communications,[1,2] optical imaging,[3] remote sensing,[4] and most recently biomedical analysis systems.[5] Among the large number of photodetectors encountered in our daily life, industry, and research, each must satisfy a certain set of requirements for a targeted application. As the light wavelength of interest spans from ultraviolet to infrared range, the energy bandgap of the semiconductor material for fabricating the photodetector must be carefully chosen to match the operating wavelength. For example, Silicon,[6] SiGe,[7] and InGaAs[8] are commonly used in optical communication systems which works in the near-infrared region, while wide-bandgap GaN, GaAlN, and SiC are mostly applied in ultraviolet detectors.[9,10] And novel semiconductor materials with varying bandgaps are constantly explored to expand the scope of applications for photodetectors.[11–14]

In the last decade, the emerging 2D layered materials have spurred intense research efforts on novel photodetectors. Different 2D materials usually possess different bandgaps, thus covering almost all the wavelengths of interest currently not achieved by traditional bulk semiconductor materials.[15,16] The layer thickness-dependent bandgap characteristics reported in many 2D materials provide an extra degree of freedom to tune the properties of photodetectors.[17,18] Further, the light absorption per layer is one order of magnitude higher than Si and the fabrication process is compatible with current semiconductor technology.[19] Thus, 2D layered materials hold great promise for implementation in photodetectors.

Early demonstrations of 2D layered materials-based photodetectors used the structure of back-gated field-effect transistor with graphene, MoS_2, or WSe_2 as the channel material.[20–22] Graphene photodetectors have been reported to have high responsivity in the infrared region. A small internal electric field in the metal–graphene junction enables ultrafast and sometimes even zero-bias operation of the photodetector.[20] However, the large dark current originating from the gapless band structure of graphene has limited its detectivity. On the other hand, photodetectors built on 2D semiconducting materials such as transition metal dichalcogenides (TMDs) and black phosphorus have the advantage of low dark current, because of the large Schottky barrier between the metal electrode and the semiconductor. In fact, an external power source is usually required to bias the device to obtain a detectable photocurrent.[21–23] For applications such as outdoor environmental sensing for wireless sensor networks, wearable medical monitoring, it is unpractical to provide or replace power source for each device,[24–26] and only self-driven or ultralow-power photodetectors are suitable.[27] Various device structures have been proposed to realize self-driven photodetectors, among them PN junction is the most studied as it can yield a substantial photocurrent without an external bias due to photovoltaic effect. As there is no reliable doping method such as ion implantation commonly used in bulk semiconductors

Dr. C. J. Zhou, Prof. B. Li
School of Electronic and Information Engineering
South China University of Technology
Guangzhou 510640, China
E-mail: zhoucj@scut.edu.cn
Dr. S. Raju, Prof. M. Chan
Department of Electronic and Computer Engineering
The Hong Kong University of Science and Technology
Kowloon 999077, Hong Kong
Prof. Y. Chai
Department of Applied Physics
The Hong Kong Polytechnic University
Kowloon 999077, Hong Kong
Prof. C. Y. Yang
Center for Nanostructures
Santa Clara University
Santa Clara, CA 95053, USA

DOI: 10.1002/adfm.201802954

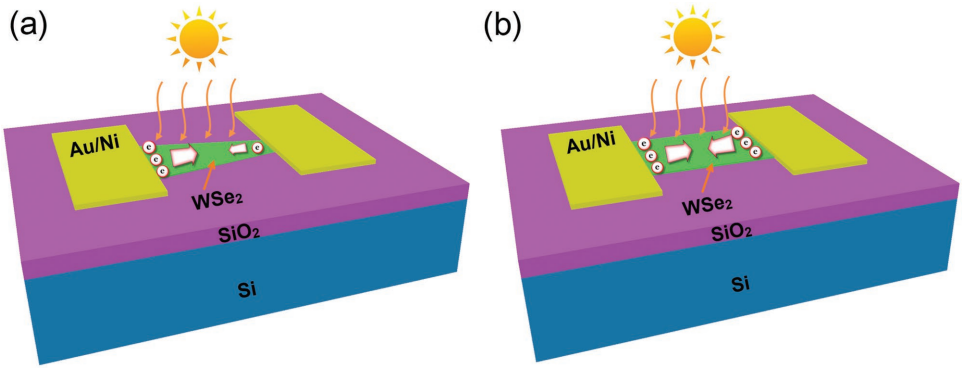

Figure 1. 3D schematic device structure of the metal-WSe_2-metal (MSM) photodetectors with a) asymmetric contact geometries, and b) symmetric contact geometries. A net current is generated when the a) device is illuminated by the light under zero bias for structure, b) while no net current results under the same condition for structure.

to achieve controllable doping in 2D materials, a double-gate structure is required to bias different parts of the channel into P and N regions, respectively, to obtain a PN junction within the channel.[28–30] Heterojunctions formed with different TMDs have also been proposed to obtain self-driven photodetectors.[12,27,31,32] Similarly, for metal–semiconductor–metal (MSM) photodetectors, different metal electrodes were introduced to obtain different Schottky barrier heights for a self-driven photodetector.[2,33] However, all these structures require complicated fabrication processes. A reliable low-cost, low dark current, and self-driven 2D materials-based photodetector is yet to be realized.

For this study, we construct MSM photodetectors based on exfoliated WSe_2 flakes. In the MSM structure, different contact lengths are chosen for the two metal–semiconductor contacts, thus forming an asymmetric contact geometry. The proposed MSM photodetector yields self-driven photoresponse characteristics with a large photocurrent under zero bias and a small dark current. Such desirable properties, together with a simple fabrication process and planar structure, make it an effective photodetector with the potential of being incorporated into various integrated circuits.

2. Device Operation Principles

Figure 1a,b illustrates the 3D schematics of the MSM photodetector with asymmetric and symmetric contact lengths, respectively. When the device is illuminated, the semiconductor material WSe_2 absorbs part of the light energy and electron–hole pairs are generated. The MSM photodetector consists of two back-to-back metal–WSe_2 junctions. For one Schottky junction, the short-circuit current under illumination is given by

$$I_{sc} = J_{sc} \times W \cdot t \tag{1}$$

where J_{sc} is the short-circuit current density, W is the contact length, and t is the WSe_2 flake thickness. J_{sc} can be expressed in terms of the open-circuit voltage of the Schottky junction

$$J_{sc} = J_{SR}\left(e^{eV_{ocMS}/\eta kT} - 1\right) \tag{2}$$

where J_{SR} is the reverse-bias saturation current density of the Schottky junction, V_{ocMS} is the open-circuit voltage of the Schottky junction, η is the ideality factor, and kT/e is the thermal voltage. As the WSe_2 flake has a uniform thickness, the Schottky barrier heights and J_{sc} of the metal–WSe_2 junction are the same for both contacts. When the incident light illuminates the whole device, the net short-circuit current is given by

$$I_{sc} = J_{sc} \times (W_R - W_L) \cdot t \tag{3}$$

where W_L and W_R are the contact lengths of the left and right metal–WSe_2 junctions, respectively. Since the junctions are back-to-back, the two short-circuit currents are opposite under illumination, and we choose the right side as the reference or the net current flows from left to right.

For an MSM device with symmetrical contact lengths as shown in Figure 1b, W_L equals W_R, and the net photocurrent is zero under zero bias. On the other hand, a net photocurrent results if the contact lengths are different (Figure 1a). For both contact geometries, the photocurrents can be enhanced by increasing the bias to increase the depletion width. Compared to the PN junction, the Schottky junction has a larger saturation current. A larger dark current is usually expected for the normal MSM photodetector because a large operating voltage needs to be applied for an achievable photocurrent. As discussed in the following section, this disadvantage can be overcome by the proposed MSM photodetector shown in Figure 1a, if the self-driven properties can be realized.

3. Results and Discussion

3.1. Electrical Characteristics

We have fabricated multiple devices with asymmetrical contact lengths based on exfoliated WSe_2 flakes. **Figure 2**a shows an optical microscope image of a fabricated MSM structure with asymmetrical contact geometries. The flake thickness used in this study is usually larger than 20 nm, which can be identified by its color on the SiO_2/Si substrate and further confirmed by atomic force microscope measurements (Figure S1, Supporting Information). Figure 2b presents the Raman and photoluminance spectrum of the WSe_2 flake. The difference between the A_{1g} and E_{2g} mode is larger than 10, and the photoluminance

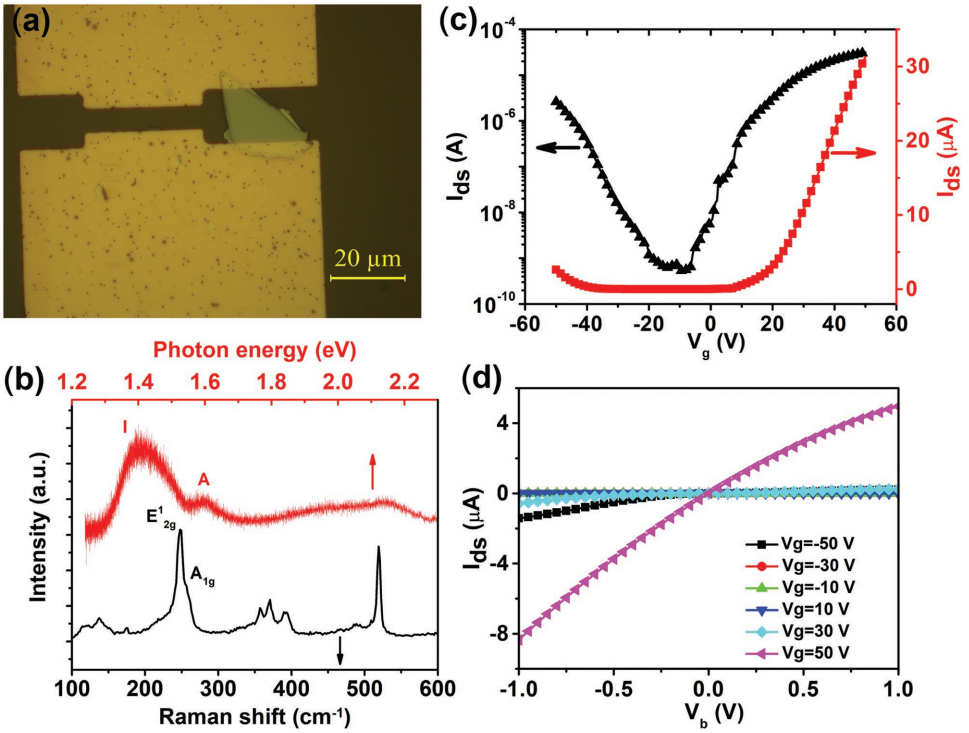

Figure 2. a) Image of a fabricated MSM photodetector with asymmetric contact geometries. b) Raman and photoluminance spectrum of a typical thick WSe_2 flake used in the MSM device fabrication. The excitation wavelength is 532 nm. c) Transfer curve of a fabricated WSe_2 device. d) Output curves of the fabricated device.

signal shows a strong peak around 1.4 eV, indicating an indirect bandgap.[34] These characteristics also confirm that the WSe_2 flake used in the device fabrication is relatively thick and bulk material constants including bandgap, dielectric constant, and effective mass can be used for device analysis.

Figure 2c shows the channel current versus gate voltage characteristics or transfer curve for a fabricated device. The silicon substrate is used as the global back gate. The device shows n-type dominant ambipolar transport properties. Due to the ambipolar characteristic of the fabricated 2D device, both electron and hole mobilities can be extracted from the measured transfer curve. The electron mobility of 26.3 cm^2 $(V \cdot s)^{-1}$ is larger than the hole mobility of 7.4 cm^2 $(V \cdot s)^{-1}$ for the present device. Similarly, the on/off ratio is about 5.82×10^4 for the n-type branch, which is larger than 4.87×10^3 for the p-type branch. At zero gate bias, there is a small electron current along the channel. Figure 2d shows the output curves of the device with the gate voltage varying between −50 and 50 V. When a gate voltage of 50 V is applied, the device shows a pronounced channel current of ≈−8 μA at $V_b = -1$ V, while it is less than 1 nA when the gate voltage is between −10 and 10 V. This clearly suggests that the device is only lightly n-type when there is no gate bias. The small channel current implies that the contact resistance is very large suggesting the existence of a large Schottky barrier formed between the metal electrodes and WSe_2. When the MSM device is used as a photodetector, no external gate bias is required. Thus, in the following photoresponse measurements, no voltage is applied to the back gate.

3.2. Self-Driven Photoresponse Characteristics

Figure 3a shows the representative current–voltage (I–V) characteristics of an MSM photodetector with asymmetric contact geometries under illumination. The full power density of the light is about 5.41 mw mm^{-2}, corresponding to a total power of 270 nW illuminated on the whole device. The light source is a 650 nm wavelength light-emitting diode. The measurement schematic is shown in the inset of Figure 3a. The metal electrode with the larger contact length is set as ground, while the bias voltage is applied to the other electrode. For varying illumination powers, the I–V curves show similar characteristics. One remarkable observation is a nonzero photocurrent I_{sc} under zero bias. Accordingly, a voltage V_{oc} needs to be applied to achieve a zero current. This phenomenon is the well-known photovoltaic effect, which is commonly observed in a PN junction or one-sided Schottky junction under illumination. Whereas in this case, this effect is caused by the asymmetric contact lengths, similar to a report on silicon using electrodes with different areas.[35] In contrast, the MSM photodetector with symmetric contact lengths shows zero I_{sc} and V_{oc} (Figure S2, Supporting Information). For the present device, a large I_{sc} of −31.1 nA and a V_{oc} of 0.16 V are obtained under a total illumination power of 270 nW. The measured V_{oc} value is not the same as V_{ocMS} in Equation (2) since V_{oc} depends on the degree of asymmetry as explained in the following sections.

Figure 3b shows the calculated responsivity, which is defined as[10,22]

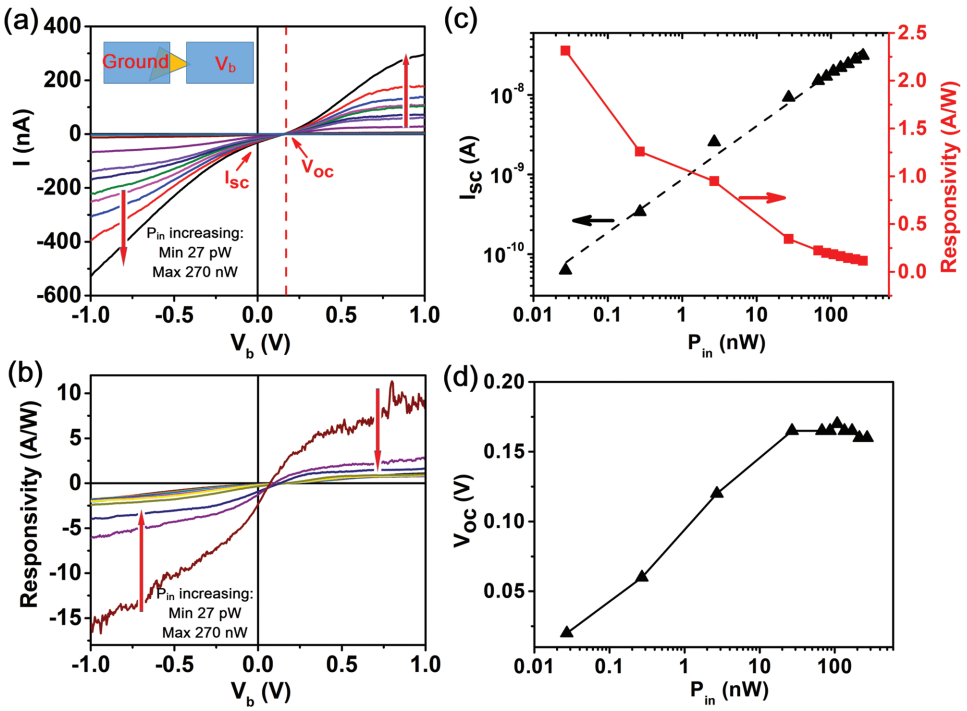

Figure 3. a) *I–V* curves of the MSM photodetector under varying light powers from 27 pW to 270 nW. The light wavelength is 650 nm. The inset shows the measurement setup. b) The calculated responsivity of the MSM photodetector for varying light powers. c) Dependence of I_{sc} and zero-biased responsivity on the light power. The dashed line is the fitting curve according to Equation (5). d) The relationship between V_{oc} and light power.

$$R = \frac{I_{ph}}{P_{in}} = \frac{I - I_D}{P_{in}} \tag{4}$$

where I is the current measured under illumination, I_D is the dark current, $I_{ph} = I - I_D$ is the photocurrent, and P_{in} is the incident light power. As in traditional MSM photodetectors, R can be enhanced with a large bias voltage V_b. The largest responsivity of 16.1 A W^{-1} is obtained with the smallest P_{in} at −1 V bias. The external quantum efficiency (EQE) is calculated using

$$\mathrm{EQE} = \frac{I_{sc}/e}{P_{in}/h\nu} \tag{5}$$

where e is the unit electronic charge, h is Planck's constant, and υ is the photon frequency. The EQE of the device at zero bias is about 22% when the incident light power is 270 nW, and it increases to 65.6% when the light power is 27 nW. We notice that the EQE could even be higher than unity for a light power decreasing to 2.7 nW, which suggests the existence of the photoconductivity gain effect in the 2D material.

Figure 3c,d shows the dependences of I_{sc} and V_{oc} on the light power. The I_{sc} exhibits a power–law relationship with the light power. The fitting curve for the relationship between I_{sc} and P_{in} is given by[14]

$$I_{sc} = cP_{in}^{\gamma} \tag{6}$$

where c is a proportionality constant and equals 8.71×10^{-10}, and γ is an empirical value and equals 0.668. This power-law relationship is commonly observed in traditional photodiodes, for which γ is equal to or less than 1.[36] The nonlinearity reflects complex charge transport involving the charge trapping and recombination, resulting in photocurrent saturation at large P_{in}. Figure 3c also presents the responsivity of the MSM photodetector under zero bias. The responsivity has an inverse relationship with the incident light power. The maximum responsivity of 2.31 A W^{-1} is obtained with P_{in} of 27 pW, which is much larger than those for TMD photodetectors under nonzero bias.[21,28] In Figure 3d, V_{oc} increases sharply from 0.02 to 0.165 V with light power increasing from 27 pW to 27 nW, and then saturates at this level (0.16–0.17 V) for even larger input powers up to 270 nW.

One disadvantage of traditional MSM photodetectors is the large dark current. For the proposed MSM photodetector with asymmetric contact geometries, ideally, a near-zero dark current is obtained at zero bias. We measure a dark current of ≈1 fA for the present device. As the resolution limit of the *I–V* measurement setup is 1 fA, when the dark current is smaller than 1 fA, it cannot be measured reliably. Thus, we use 1 fA as the dark current value in the ensuing calculations. The measured periodic I_{sc} curve of the photodetector is shown in Figure S3 in the Supporting Information. The short-circuit photocurrent I_{on} is above 650 pA, and the dark current can reach to a value of ≈1 fA when it is stabilized. Thus, the estimated I_{on}/I_{dark} ratios of the MSM photodetector are larger than 10^5 at zero bias.

One important performance parameter of a photodetector related to dark current is detectivity, given by[22]

$$D^* = \frac{A^{1/2}R}{(2eI_D)^{1/2}} \tag{7}$$

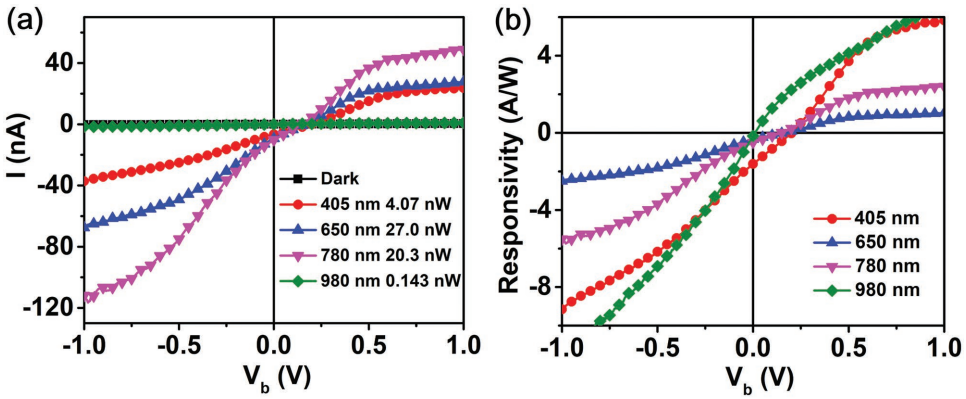

Figure 4. a) Measured *I–V* curves of asymmetric MSM photodetector under illumination at different light wavelengths. b) The calculated responsivity of the MSM photodetector.

where A is the device area and I_D is the dark current. For a P_{in} of 27 pW, the detectivity is estimated to be about 9.16×10^{11} Jones ($A = 50.3\ \mu m^2$, $R = 2.31$ A W^{-1}, and $I_D = 1$ fA), which is among the highest reported values for TMD photodetectors.[22]

Broadband photoresponse is also investigated for the proposed MSM photodetector. In the measured wavelength range of 405–980 nm, the MSM photodetector shows similar self-driven characteristics, as manifested by the I_{sc} and V_{oc} shown in **Figure 4**a. V_{oc} increases with increasing photon energy, with the highest value of 0.2 V obtained at a wavelength of 405 nm and P_{in} of 4.07 nW. Although V_{oc} is only 0.01 V at 980 nm wavelength, it is mainly due to the small P_{in} (143 pW) used. Figure 4b reveals that the largest responsivity of 11.2 A W^{-1} is obtained at −1 V with such a small P_{in}. In general, Figure 4b shows that a high responsivity with magnitude larger than 2 A W^{-1} is obtained at a bias of −1 V for all photon wavelengths used. For zero bias responsivity, the largest value of 1.62 A W^{-1} is obtained at 405 nm.

It is important to correlate the self-driven characteristic with the degree of contact asymmetry. Here we use contact length difference (ΔCL) as a measure of the degree of asymmetry. **Figure 5**a shows the *I–V* curves for MSM photodetectors with different asymmetric contact geometries. One observation is the broad range of V_{oc}, from 0 to 0.42 V. Figure 5b shows the relationship between V_{oc} and ΔCL. The images of the corresponding devices are shown in Figure S4 (Supporting Information) to reveal the exact geometries of the MSM photodetectors. In general, a larger ΔCL results in a higher V_{oc}. The near-zero V_{oc} is obtained with a device with near-identical contact lengths (6.043/6.036 μm), and the highest V_{oc} of 0.42 V is from a device with the largest ΔCL (23.783/2.192 μm). We note that V_{oc} is not exactly proportional to ΔCL, suggesting that other parameters such as channel length and contact interface might also be determining factors.

Since the first demonstrations of the photodetectors based on the single-layer MoS_2 flake,[21,37] various photodetectors based on TMD materials have been reported to exhibit superior properties.[38–41] We note that CVD synthesized 2D materials usually have triangular or other irregular shapes. However, these photodetectors have not realized or utilized the effect of asymmetrical contacts for self-driven photodetectors. It is important to point out that the photovoltaic effect induced by asymmetrical contacts depends on two important factors, the degree of contact asymmetry and the metal-semiconductor barrier height.

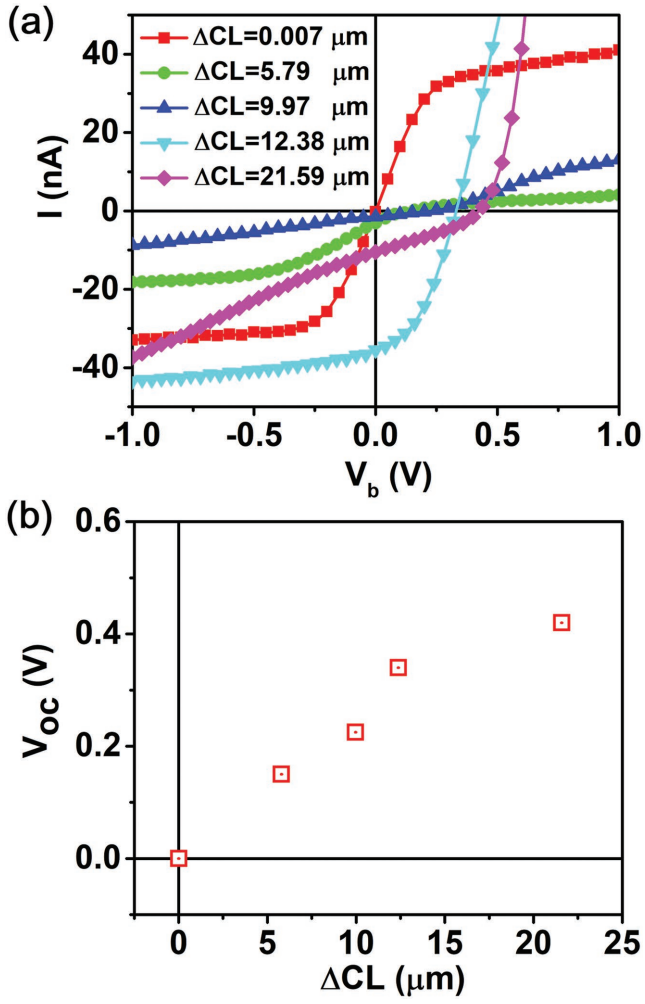

Figure 5. a) *I–V* curves of multiple MSM photodetectors with different degrees of asymmetries. b) The relationship between contact length difference (ΔCL) and V_{oc} of the MSM photodetectors.

3.3. Modeling and Analysis of the MSM Photodetector

We further analyze the operation of the proposed MSM photodetector to identify the origin of the self-driven characteristics. From the transfer curve in Figure 2c, we confirm that the WSe_2 flakes used in this work are n-type when there is no gate bias. With an applied bias V_b between the two electrodes, the photocurrent first follows a linear relationship with V_b and then saturates at a voltage of between about 0.5 and 1 V, depending on incident light power (Figure 3a). The saturation voltage increases with increasing light power, due to Schottky barrier lowering under high-power illumination. For a small P_{in}, photocurrent saturation occurs when the channel is fully depleted, and the saturation voltage is expressed as[42,43]

$$V_{Sat} = \left(\frac{qN_D}{2\varepsilon_s}\right)s^2 \tag{8}$$

Here, N_D is the doping concentration, ε_s is the dielectric constant of WSe_2, and S is the channel length which is about 10 µm in this device. The dielectric constant is 20 at a light wavelength of 633 nm. Then a doping concentration of $\approx 10^{13}$ cm^{-3} is obtained. Using these parameters, we develop a finite-element model (FEM) for the MSM photodetectors with both symmetric and asymmetric contact geometries. Details of the device structures used in the FEM are given in Figure S5 in the Supporting Information. For the MSM photodetector with symmetric contacts, the contact lengths are set at 5 µm and the channel length is 2 µm. For the device with asymmetric contacts, we only change one contact length to be less than 5 µm. In the process of calculating the I–V characteristics, we have adopted an ideal Schottky contact model for the metal–WSe_2 junction.

We first examine the origin of the net current of the MSM photodetector at zero bias. **Figure 6**a shows the electric field distribution of the MSM photodetector with a contact length difference of 4.5 µm under 650 nm light illumination. As the magnitudes of the built-in electric field near the contacts for both sides are the same but with opposite direction (Figure S6a, Supporting Information), the resulting photocurrent densities near the contacts, which are due to the sweeping of the photogenerated carriers by the built-in electric field, should be the same in magnitude and opposite in direction. As a result, a net current is obtained for the MSM photodetector with asymmetric contact lengths. Figure 6b shows the arrow surface plot of the photocurrent density distribution for the asymmetric device with a contact length difference of 4.5 µm. The net current is −83.7 nA, in which the minus sign means

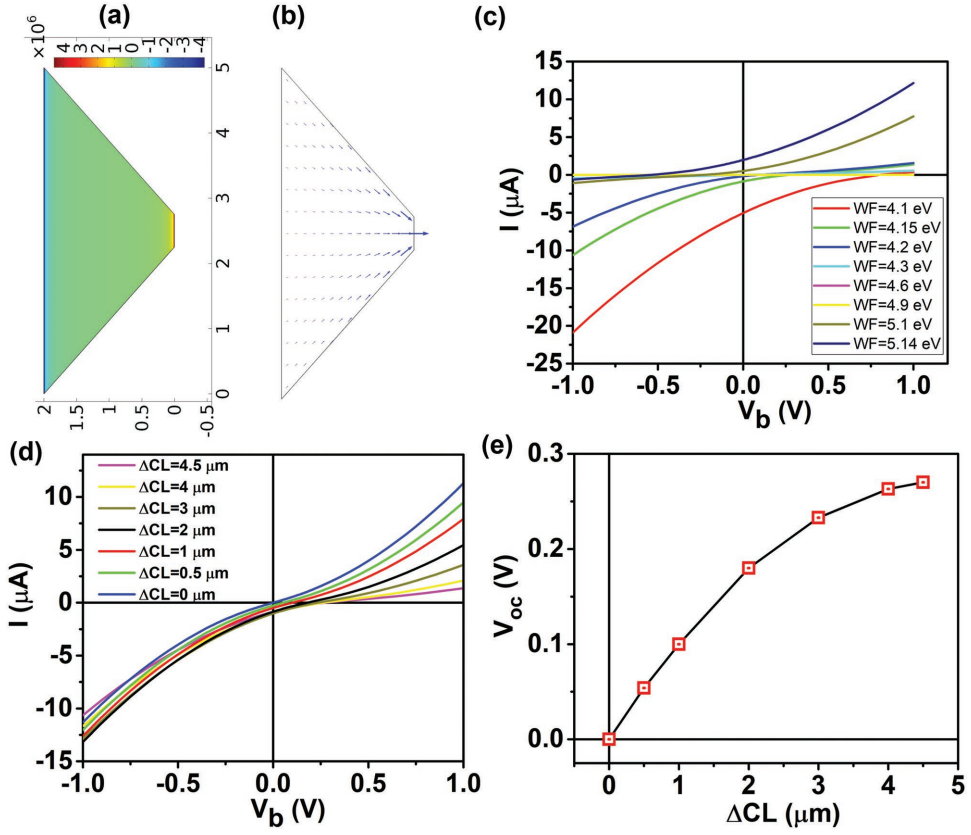

Figure 6. a) Calculated electric field distribution of the MSM photodetector with ΔCL = 4.5 µm at zero bias. b) Current density distribution of the MSM photodetector in inset (a) at zero bias, with the magnitude and direction of the current represented by the arrow length and direction, respectively. c) I–V curves of the asymmetric MSM photodetector with various metal electrode work functions. The narrower contact length is 0.5 µm. The metal work function varies between 4.1 and 5.14 eV. d) I–V curves of the asymmetric MSM photodetector with various contact length differences. The narrower contact length is between 0.5 and 5 µm. e) Dependence of V_{oc} on the contact length difference.

the current is flowing from the wider electrode to the narrower electrode. In the case of the symmetric device, a near zero current (0.65 pA) is obtained. This negative I_{sc} implies that the energy band bends toward the metal (Figure S6b, Supporting Information), i.e., the electric field points from the metal to WSe_2.

It is noteworthy that the Schottky barrier is necessary for the self-driven characteristics. We have studied the evolution of I_{sc} and V_{oc} with the metal work function. A large negative I_{sc} of 5.06 μA along with a large V_{oc} of 0.8 V is obtained for the photodetectors with a metal work function of 4.1 eV. I_{sc} becomes positive as the metal work function increases to 4.8 eV. In the case of a metal work function of 5.14 eV, I_{sc} is 1.97 μA and the V_{oc} is −0.55 V. For both cases, a large Schottky barrier is formed. Comparing this analysis to our experimental results, the metal Fermi level in the proposed device structure should be above that of WSe_2. In general, a large Schottky barrier is required if large I_{sc} and V_{oc} are desirable.

Further, we explore the dependence of I_{sc} and V_{oc} on the contact asymmetry. Figure 6d compares the calculated I–V curves of the MSM photodetectors with various narrower contact lengths while keeping the other contact length at 5 μm. I_{sc} increases from −0.6 pA to ≈−1 μA, when ΔCL varies from zero to 4.5 μm. Figure 6e shows the relationship between V_{oc} and ΔCL, which has a similar trend as the experimental results. For a small ΔCL, the V_{oc} follows a linear relationship with ΔCL, and it saturates at a larger value.

4. Conclusion

We propose a novel MSM WSe_2 photodetector which shows self-driven characteristics. The MSM photodetector has an asymmetric contact geometry, which results in a net current flow without external bias. For the present device, a high responsivity of 2.31 A W^{-1} is obtained at zero bias. The proposed MSM photodetector can overcome the disadvantage of the high dark current present in existing MSM photodetectors. A small dark current of ≈1 fA along with a high detectivity of 9.16×10^{11} Jones, and a high on/off current ratio are achieved. The MSM photodetector also shows self-driven broadband photoresponse in the range of 405–980 nm. We have also performed a finite-element analysis to study the origin of the self-driven characteristics, and qualitatively confirm the dependence of the self-driven performance on the degrees of asymmetry. The coplanar device structure and the much simpler fabrication process than traditional self-driven devices like PN junction suggest the promising applications of the proposed MSM photodetectors with asymmetric contact geometries.

5. Experimental Section

Device Fabrication: For the sample preparation, we used the SiO_2 (300 nm)/Si wafer as the starting substrate. The WSe_2 flakes were transferred to the SiO_2/Si wafer by mechanical exfoliation method. Then we checked the transferred flakes and identified the WSe_2 flakes with special shapes like triangular shape or those with sharp angles for fabricating the MSM devices with asymmetrical contact geometries. The electrode pattern was aligned with the chosen WSe_2 flakes in such a way that two electrodes have very different contact lengths. Au (50 nm)/Ni (10 nm) were subsequently deposited on the substrate at a rate of 1 Å s^{-1} by electron beam evaporation method. At last, lift-off in acetone is performed to form the MSM photodetectors.

Electrical and Photoresponse Characterization: The electrical performances of the devices are characterized by a semiconductor parameter analyzer Agilent 4156c. The measurements were conducted in ambient without light illumination. For the photoresponse measurements, the light is illuminated on the entire device through a microscope equipped with the probe station for current–voltage (I–V) measurements. A laser diode with varying wavelengths was used to illuminate the whole device through a focused objective. With a 20× objective used in the experiment, the diameter of the focused spot size is about 1 mm, which is much larger than our flake size and ensuring the illumination is global. The power of the light illuminated on the device is tuned by an attenuator with different light losses. The total power of the light illuminated on the substrate is measured with a New-port power meter, and the effective input power illuminated on the entire device is calculated by considering the area of the WSe_2 flake and the area of the light spot of the objective.

Finite Element Analysis: 2D finite element modeling and analysis are performed with COMSOL software by coupling the semiconductor interface with electromagnetic waves. The material constants of the semiconductor (WSe_2) are from multiple references, including energy bandgap,[34] refractive index and extinction coefficient,[44,45] and dielectric constant,[46] electron affinity,[47] and effective mass and equivalent density of states.[48] For the channel contact lengths, the wider side is set as 5 μm, and the other side varying between 0.5 and 5 μm. A channel length of 2 μm is adopted in the simulation considering the computation efficiency and results visualization. I–V curves can be derived by applying a bias voltage to the narrower side, which is the same as the experimental measurement setup.

Supporting Information

Supporting Information is available from the Wiley Online Library or from the author.

Acknowledgements

This research was supported by the Science and Technology Program of Guangzhou (201804010393); International Science & Technology Cooperation Plan in Science and Technology Program of Guangzhou (201807010072); the Planned Science and Technology Project of Guangdong Province, China (2015B090901048, 2017B090901068); and Research Grant Council of Hong Kong (PolyU 152145/15E).

Conflict of Interest

The authors declare no conflict of interest.

Keywords

2D materials, low dark current, metal–semiconductor–metal, self-driven photodetectors

Received: April 30, 2018
Revised: July 12, 2018
Published online:

[1] P. C. Eng, S. Song, B. Ping, *Nanophotonics* **2015**, *4*, 277.
[2] T. Mueller, F. Xia, P. Avouris, *Nat. Photonics* **2010**, *4*, 297.
[3] M. Engel, M. Steiner, P. Avouris, *Nano Lett.* **2014**, *14*, 6414.

[4] R. Szedlak, A. Harrer, M. Holzbauer, B. Schwarz, J. P. Waclawek, D. MacFarland, T. Zederbauer, H. Detz, A. M. Andrews, W. Schrenk, B. Lendl, G. Strasser, *ACS Photonics* **2016**, *3*, 1794.
[5] W. W. Moses, *Nucl. Instrum. Methods Phys. Res. A* **2009**, *610*, 11.
[6] G. Li, K. Maekita, H. Mitsuno, T. Maruyama, K. Iiyama, *Jpn. J. Appl. Phys.* **2015**, *54*, 04DG06.
[7] L. Kuang-Sheng, H. Ji-Chen, K. Y. J. Hsu, *IEEE Electron Device Lett.* **2007**, *28*, 800.
[8] Z. Sheng, L. Liu, J. Brouckaert, S. He, D. Van Thourhout, *Opt. Express* **2010**, *18*, 1756.
[9] H. Jiang, T. Egawa, H. Ishikawa, C. Shao, T. Jimbo, *Jpn. J. Appl. Phys.* **2004**, *43*, L683.
[10] S.-X. Liu, T. Wang, Z.-Z. Chen, *IEEE Electron Device Lett.* **2017**, *38*, 1405.
[11] X. Jing, E. Panholzer, X. Song, E. Grustan-Gutierrez, F. Hui, Y. Shi, G. Benstetter, Y. Illarionov, T. Grasser, M. Lanza, *Nano Energy* **2016**, *30*, 494.
[12] Z. Xu, S. Lin, X. Li, S. Zhang, Z. Wu, W. Xu, Y. Lu, S. Xu, *Nano Energy* **2016**, *23*, 89.
[13] Y. Dai, X. Wang, W. Peng, C. Wu, Y. Ding, K. Dong, Z. L. Wang, *Nano Energy* **2018**, *44*, 311.
[14] D. Zheng, H. Fang, P. Wang, W. Luo, F. Gong, J. C. Ho, X. Chen, W. Lu, L. Liao, J. Wang, W. Hu, *Adv. Funct. Mater.* **2016**, *26*, 7690.
[15] F. H. Koppens, T. Mueller, P. Avouris, A. C. Ferrari, M. S. Vitiello, M. Polini, *Nat. Nanotechnol.* **2014**, *9*, 780.
[16] C. Xie, Y. Wang, Z.-X. Zhang, D. Wang, L.-B. Luo, *Nano Today* **2018**, *19*, 41.
[17] C. Zhou, Y. Zhao, S. Raju, Y. Wang, Z. Lin, M. Chan, Y. Chai, *Adv. Funct. Mater.* **2016**, *26*, 4223.
[18] A. Ciarrocchi, A. Avsar, D. Ovchinnikov, A. Kis, *Nat. Commun.* **2018**, *9*, 919.
[19] M. Bernardi, M. Palummo, J. C. Grossman, *Nano Lett.* **2013**, *13*, 3664.
[20] F. Xia, T. Mueller, Y. M. Lin, A. Valdes-Garcia, P. Avouris, *Nat. Nanotechnol.* **2009**, *4*, 839.
[21] Z. Yin, H. Li, H. Li, L. Jiang, Y. Shi, Y. Sun, G. Lu, Q. Zhang, X. Chen, H. Zhang, *ACS Nano* **2012**, *6*, 74.
[22] C. Xie, C. Mak, X. Tao, F. Yan, *Adv. Funct. Mater.* **2017**, *27*, 1603886.
[23] M. Huang, M. Wang, C. Chen, Z. Ma, X. Li, J. Han, Y. Wu, *Adv. Mater.* **2016**, *28*, 3481.
[24] Z. L. Wang, *Adv. Mater.* **2012**, *24*, 280.
[25] Z. L. Wang, W. Wu, *Angew. Chem., Int. Ed. Engl.* **2012**, *51*, 11700.
[26] Y. Ma, Q. Zheng, Y. Liu, B. Shi, X. Xue, W. Ji, Z. Liu, Y. Jin, Y. Zou, Z. An, W. Zhang, X. Wang, W. Jiang, Z. Xu, Z. L. Wang, Z. Li, H. Zhang, *Nano Lett.* **2016**, *16*, 6042.
[27] W. Tian, Y. Wang, L. Chen, L. Li, *Small* **2017**, *13*, 1701848.
[28] B. W. Baugher, H. O. Churchill, Y. Yang, P. Jarillo-Herrero, *Nat. Nanotechnol.* **2014**, *9*, 262.
[29] M. C. Lemme, F. H. Koppens, A. L. Falk, M. S. Rudner, H. Park, L. S. Levitov, C. M. Marcus, *Nano Lett.* **2011**, *11*, 4134.
[30] Y. Q. Bie, G. Grosso, M. Heuck, M. M. Furchi, Y. Cao, J. Zheng, D. Bunandar, E. Navarro-Moratalla, L. Zhou, D. K. Efetov, T. Taniguchi, K. Watanabe, J. Kong, D. Englund, P. Jarillo-Herrero, *Nat. Nanotechnol.* **2017**, *12*, 1124.
[31] H. M. Li, D. Lee, D. Qu, X. Liu, J. Ryu, A. Seabaugh, W. J. Yoo, *Nat. Commun.* **2015**, *6*, 6564.
[32] X. Zhou, X. Hu, J. Yu, S. Liu, Z. Shu, Q. Zhang, H. Li, Y. Ma, H. Xu, T. Zhai, *Adv. Funct. Mater.* **2018**, *28*, 1706587.
[33] M. Fontana, T. Deppe, A. K. Boyd, M. Rinzan, A. Y. Liu, M. Paranjape, P. Barbara, *Sci. Rep.* **2013**, *3*, 1634.
[34] H. Sahin, S. Tongay, S. Horzum, W. Fan, J. Zhou, J. Li, J. Wu, F. M. Peeters, *Phys. Rev. B* **2013**, *87*, 165409.
[35] M. G. Rabbani, J. P. Sundararajan, A. Verma, R. Nekovei, M. M. Khader, R. B. Darling, S. R. Patil, *Semicond. Sci. Technol.* **2017**, *32*, 015001.
[36] H. Lu, X. Zhou, T. Liang, L. Zhang, S. Zhang, *Appl. Phys. Lett.* **2018**, *112*, 042103.
[37] O. Lopez-Sanchez, D. Lembke, M. Kayci, A. Radenovic, A. Kis, *Nat. Nanotechnol.* **2013**, *8*, 497.
[38] N. Perea-López, Z. Lin, N. R. Pradhan, A. Iñiguez-Rábago, A. Laura Elías, A. McCreary, J. Lou, P. M. Ajayan, H. Terrones, L. Balicas, M. Terrones, *2D Mater.* **2014**, *1*, 011004.
[39] J. Xia, X. Huang, L.-Z. Liu, M. Wang, L. Wang, B. Huang, D.-D. Zhu, J.-J. Li, C.-Z. Gu, X.-M. Meng, *Nanoscale* **2014**, *6*, 8949.
[40] C. Jung, S. M. Kim, H. Moon, G. Han, J. Kwon, Y. K. Hong, I. Omkaram, Y. Yoon, S. Kim, J. Park, *Sci. Rep.* **2015**, *5*, 15313.
[41] S. Lei, L. Ge, Z. Liu, S. Najmaei, G. Shi, G. You, J. Lou, R. Vajtai, P. M. Ajayan, *Nano Lett.* **2013**, *13*, 2777.
[42] D. S. Tsai, D. H. Lien, M. L. Tsai, S. H. Su, K. M. Chen, J. J. Ke, Y. C. Yu, L. J. Li, J. H. He, *IEEE J. Sel. Top. Quantum Electron.* **2014**, *20*, 30.
[43] M. Casalino, M. Iodice, L. Sirleto, I. Rendina, G. Coppola, *Opt. Express* **2013**, *21*, 28072.
[44] Y. Li, A. Chernikov, X. Zhang, A. Rigosi, H. M. Hill, A. M. van der Zande, D. A. Chenet, E.-M. Shih, J. Hone, T. F. Heinz, *Phys. Rev. B* **2014**, *90*, 205422.
[45] S. S. Rassay, *Master Thesis*, New Jersey Institute of Technology **2017**.
[46] Q. Ouyang, S. Zeng, L. Jiang, L. Hong, G. Xu, X. Q. Dinh, J. Qian, S. He, J. Qu, P. Coquet, K. T. Yong, *Sci. Rep.* **2016**, *6*, 28190.
[47] R. Schlaf, O. Lang, C. Pettenkofer, W. Jaegermann, *J. Appl. Phys.* **1999**, *85*, 2732.
[48] G. V. Resta, T. Agarwal, D. Lin, I. P. Radu, F. Catthoor, P. E. Gaillardon, G. De Micheli, *Sci. Rep.* **2017**, *7*, 45556.